

This Page Is Inserted by IFW Operations
and is not a part of the Official Record

BEST AVAILABLE IMAGES

Defective images within this document are accurate representations of the original documents submitted by the applicant.

Defects in the images may include (but are not limited to):

- BLACK BORDERS
- TEXT CUT OFF AT TOP, BOTTOM OR SIDES
- FADED TEXT
- ILLEGIBLE TEXT
- SKEWED/SLANTED IMAGES
- COLORED PHOTOS
- BLACK OR VERY BLACK AND WHITE DARK PHOTOS
- GRAY SCALE DOCUMENTS

IMAGES ARE BEST AVAILABLE COPY.

**As rescanning documents *will not* correct images,
please do not report the images to the
Image Problem Mailbox.**

THIS PAGE BLANK (USPTO)

PORVAIR FUEL CELL TECHNOLOGY

FLUID PROPERTIES OF OPEN CELL SINTERED IRON BASED POROUS METAL STRUCTURES

EXPERIMENTAL RESULTS AND DISCUSSION

Don Floyd

Sr. Product Development Engineer

Porvair Fuel Cell Technology

JULY 2001

PROPERTIES OF OPEN CELL SINTERED IRON BASED POROUS METAL STRUCTURES

EXPERIMENTAL RESULTS AND DISCUSSION

INTRODUCTION

Metal foams are a new class of materials with low densities and novel physical, mechanical, thermal, electrical, and acoustic properties. They offer potential in fuel cell systems for thermal management, catalyst support, filtration, steam generation, mixing, energy absorption, acoustic absorption, and filters as well as applications in the cell stack assembly as bi-polar plates and gas diffusion. Metal foams also hold particular promise in applications where several of these features can be exploited simultaneously.

Porvair Fuel Cell Technology produces a variety of porous structures (Figures 1&2). The base materials used to make them can be most any powder metal (or ceramic), the void fraction and pore size can be controlled independently of one another, and virtually any shape can be manufactured. The pore sizes can range from about 0.2 inches to 10 microns and the void fraction can range from about 97% to 80% (3% relative density to 20% relative density). This wide range of base materials and properties guarantees a product that can fit in most any application.

Figure1: FeCrAlY Metal Foams in Catalyst Substrate and Heat Exchange Applications

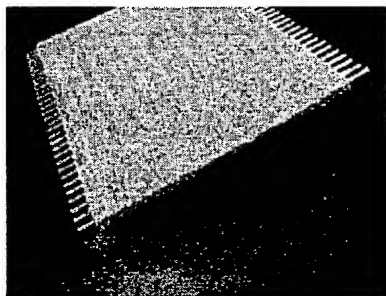


Figure2: Copper, Brass, FeCrAlY, Nickel, Titanium and Stainless Steel Metal Foam



Controlling the material properties is very important for many different reasons. For instance, a very small pore size has a larger surface area for catalytic applications than a large pore size, but comes with the cost of a higher pressure drop. A foam structure with a high relative density has better conductive and convective heat transfer properties as well as greater strength than foam with a low relative density. But an increase in relative density means a heavier component with a slower time response in thermal applications.

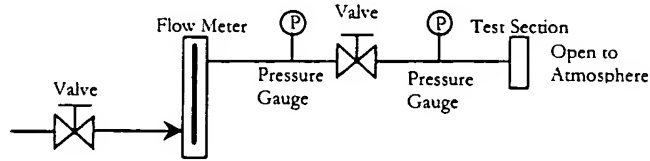
In order to use metal foams effectively, the interaction between the physical characteristics (relative density, pore size, material type) and the material properties (strength, pressure drop, surface area) must be understood. This paper attempts to present the properties in a way that facilitates comparison with other materials and structures, summarizes the guidelines for design with metal foams, and illustrates how they might be used in fuel cell applications.

PRESSURE DROP IN IRON BASED METAL FOAMS

Experimental Setup and Procedure

The pressure drop tests apparatus is shown schematically in Figure 3, it consists of a flow meter, pressure gauges, and hand operated valves. Air flows through the inlet pipe which is four inches in diameter and 30 inches long. The inlet pipe terminates at the test section, where the specimen is loaded. The specimen is placed into a gasket, to ensure the air flows in the axial direction, and is secured with a pneumatic clamping system. The two valves shown in Figure 3 are adjusted until the desired flow rate is obtained. The inlet and exit pressures are noted as well as the flow rate. Based on the results from the measurements, the pressure drop as a function of velocity is obtained.

Figure 3: Test Apparatus Schematic



Equation Development

Darcy may have been the first to examine flow through porous media. Darcy [1] described his empirical studies on steady-state filtration demonstrating that the water volume passing through a sand layer is proportional to the pressure-drop across the length of the layer, leading to the equation

$$\alpha = \frac{U^*}{\left(\frac{\Delta P^*}{L^*}\right)}, \quad (1)$$

where α is the hydraulic conductivity of the porous medium, U^* is the channel cross-section average speed, and ΔP^* is the hydrostatic pressure difference across the layer of length L^* .

Several steps have been taken to generalize Eq. (1). Hazen [2] unveiled the fluid viscosity effect on the original flow equation proposed by Darcy, Eq. (1). By altering the temperature of the fluid before entering the medium, he observed the influence of the temperature on the hydraulic conductivity calculated using Eq. (1). He proposed a modification to the original equation of the form

$$U^* = \left(\frac{T^* + 10}{60}\right) \alpha_{50} \frac{\Delta P^*}{L^*}, \quad (2)$$

where T^* is the water temperature, measured in degrees Fahrenheit, and α_{50} is the reference hydraulic conductivity value measured when the water is 50°F.

Inspection of Eq. (2) reveals that the correction $60/(T^*+10)$ mimics the water viscosity dependence on temperature, $\mu(T^*)/\mu(50^\circ\text{F})$, to less than one percent. Therefore, it is reasonable to rewrite Eq. (2) as

$$U^* = \frac{K}{\mu(T^*)} \frac{\Delta P^*}{L^*}, \quad (3)$$

where $K=[\mu(50^\circ\text{F}) \alpha_{50}]$, known as the specific permeability, is a parameter supposedly independent of fluid properties.

Dupuit [3] was the first scientist to use theoretical principles to interpret Darcy's equation [4]. A consequence of Dupuit's study is the inclusion of a quadratic velocity term added to Eq. (3) modeling the resistive form drag imposed on the fluid by the solid permeable medium

$$\frac{\Delta P^*}{L^*} = \frac{\mu(T^*)}{K} U^* + C \rho U^{*2}, \quad (4)$$

where the coefficient C is the form coefficient of the porous layer. Eq. (4) is referred to as the Hazen-Dupuit-Darcy equation [4].

In an internal technical memo [5], J.A.F. Hill reported the development of an equation to predict the pressure-drop across a porous-metal filter as a function of fluid flow. The pressure-drop data was gathered by flowing air through a porous metal sheet. The origin of the equation can be found in publications by Forscheimer and Reynolds. In the basic equation,

$$-\rho \frac{\partial P^*}{\partial x} = \frac{\mu(T^*)}{K} \dot{m}^* + C \dot{m}^{*2}, \quad (5)$$

\dot{m}^* is the mass flow rate, and all other variables are as mentioned before with a slightly different interpretation. The first constant, K , in Eq. 5 is called the inertial resistance coefficient and is analogous to the specific permeability. The second constant, C , is called the viscous resistance coefficient and is analogous to the form coefficient. At low flow rates the contribution of the C term is negligible, but as the flow rate increases, the contribution of C is significant. At very high flows C dominates the pressure drop relationship.

By rearranging Eq. (5) and using the equation of state for ideal gas, $P=\rho RT$, we get

$$-P^* dP^* = \left(\frac{\mu RT}{K} \dot{m} + CRT \dot{m}^2 \right) dx. \quad (6)$$

Integrating Eq. (6) across the bed length, L^* , and assuming constant fluid viscosity gives

$$\frac{P_{in}^2 - P_{L^*}^2}{L^*} = \frac{2\mu RT}{K} \dot{m} + 2RTC \dot{m}^2. \quad (7)$$

Rearranging Eq. (7) yields

$$\frac{\Delta P^*}{L^*} \left(1 - \frac{1}{2} \frac{\Delta P^*}{P_{in}} \right) = \frac{\mu}{K} AU^* + C\rho_{in}(AU^*)^2, \quad (8)$$

but according to M.J. Rosso Jr. et al [6], Eq. (8) takes the form

$$\frac{\Delta P^2}{L^*} = \frac{\mu RT\rho}{K} U^* + CRT\rho U^{*2} \quad (9)$$

after “suitable fitting to measured results”. Rosso et al indicates that K is a function of the system geometry as well as the characteristics of the porous material. Unlike Eq. 4, Eq. 9 implies that ΔP^2 is proportional to $C_1 U^* + C_2 U^{*2}$ rather than ΔP .

Rosso et al also indicates that K should be proportional to $1/D_p^2$ and $\rho_{rel}^2/(1-\rho_{rel})^3$. Where D_p is the particle diameter and ρ_{rel} is the relative density (1 minus the void fraction) of the porous material. It should be noted that the experiments by Rosso et al were conducted on porous metal *sheets* not metal foam structures. The particle diameter, D_p , does not play a significant role in the pressure drop of foam structures; the pressure drop is primarily driven by the open pore size (cell size).

In the book, *Metal Foams: A Design Guide* Ashby et al [6] show the pressure drop as

$$\frac{\Delta P}{L} = \xi \frac{1}{a} \left[\frac{v_a^m \rho_a}{(1-\alpha)^{2-m}} \right] U_f^{2-m} d^{-m} \quad (10)$$

where a is the metal foam cell size, v_a is the fluid kinematic viscosity, ρ_a is the fluid density, α is the fluid thermal diffusivity, U is the free steam velocity, and d is the ligament diameter (or strut diameter). The exponent m and the coefficient ξ are determined experimentally.

For the purposes of this study, Eq. 10 was rewritten with ppi number and relative density. We know that the ligament diameter is inversely proportional to the ppi number and the relative density. Also, the metal foam cell size, a , is inversely proportional to the ppi number and relative density. Therefore Eq. 10 is rewritten as

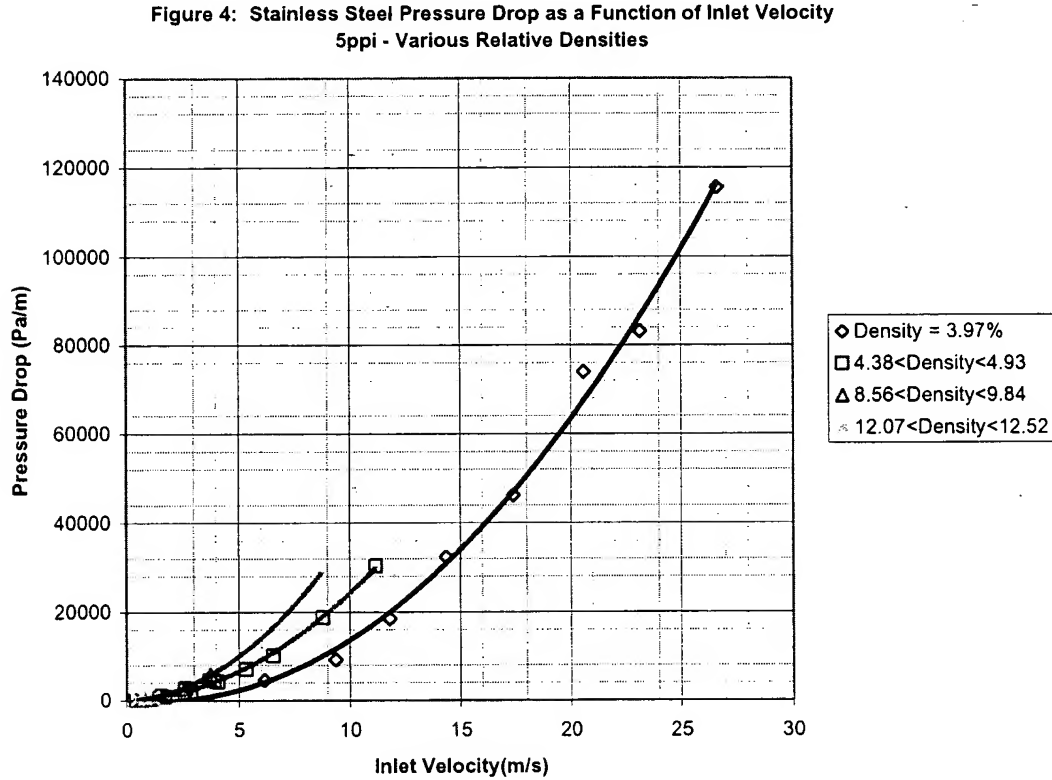
$$\frac{\Delta P}{L} = \hat{\xi} (ppi)^t \left[\frac{v_a^{\hat{m}} \rho_a}{(1-\alpha)^{2-\hat{m}}} \right] U_f^{2-\hat{m}} \rho_{rel}^{\hat{n}} \quad (11)$$

Equations 4, 9, and 11 are utilized and the results are compared in order to shown the dependence of pressure drop on the free steam fluid velocity, the relative density, and the ppi number.

Experimental Results For Constant Inlet and Exit Diameter

Scrutiny of Eq. 4

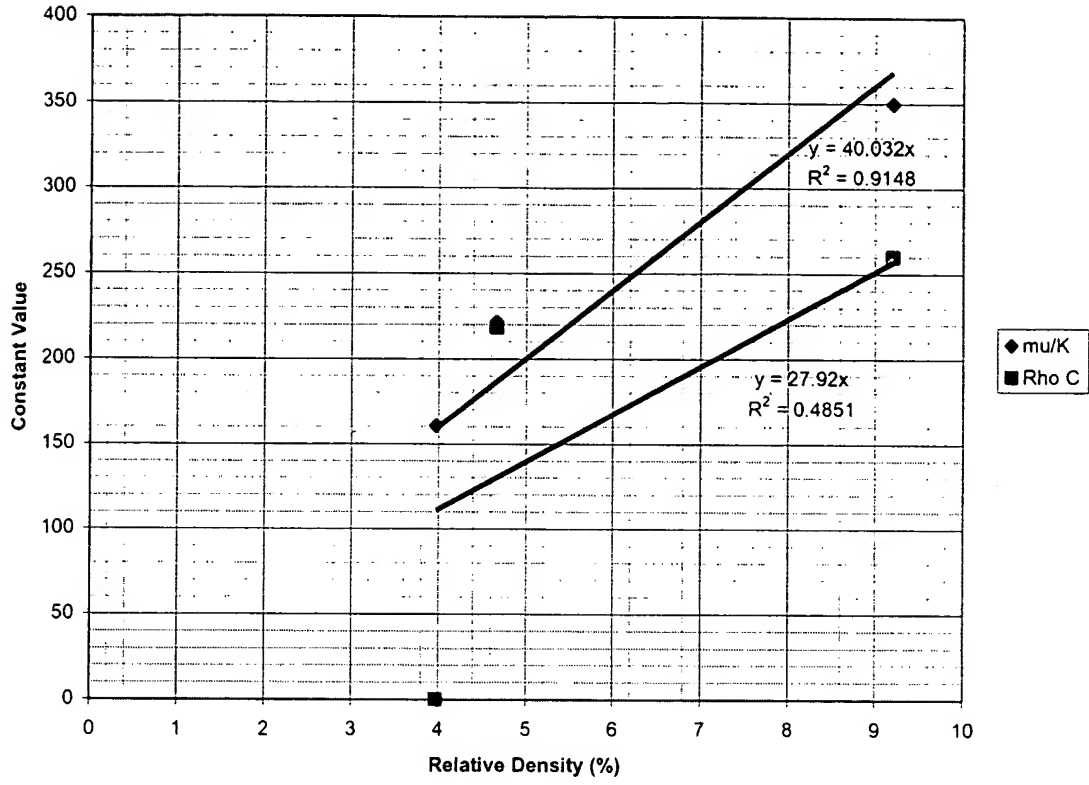
Nearly 180 runs were conducted with stainless steel samples of different diameter, thickness, inlet velocity, ppi, and relative density. Equations 4, 9, and 11 are utilized and the results are compared to show the best fit for the data. Figure 4 shows the interaction between the pressure drop and the inlet velocity for 5 ppi stainless steel foam with different relative densities. The same plots were created for 10, 20, 30, 40, 50, 60, and 80 ppi foams with similar results and are located in Appendix I. The



solid lines are a quadratic least squares fit of the data and show an average coefficient of determination value of 99.6%, indicating that the model relating pressure drop to the velocity can account for 99.6% of the variation present in the sample of pressure drop values. Moreover, the qualitative results from the curve fit shown that as the ppi number and relative density increase so do the coefficients $1/K$ and C in Eq. 4. The quantitative results of the curve fit in conjunction with the qualitative results tend to validate the use of Eq. 4.

The values of μ/K and ρC were computed at various densities for each ppi number. The values are tabulated in Appendix II and show an increase in the two constants as the relative density is increased and as the ppi number is increased. The constants were then fit to the relative density at each ppi number. Figure 5 shows the relationship between the relative density and μ/K , as well as the relative density and ρC at 5 ppi.

Figure 5: μ/K and ρC as a Function of Relative Density



A linear dependence of μ/K and ρC on the relative density was initially assumed. This lead to the equations:

$$\frac{\mu}{K} = \alpha_1 \rho_{rel} \quad (12)$$

and

$$C\rho = \alpha_2 \rho_{rel}, \quad (13)$$

where α_1 and α_2 are functions of the ppi number. The coefficients α_1 and α_2 were then fit to the ppi number with the results shown in Figure 6 and Figure 7.

Figure 6: α_1 as a Function of PPI Number

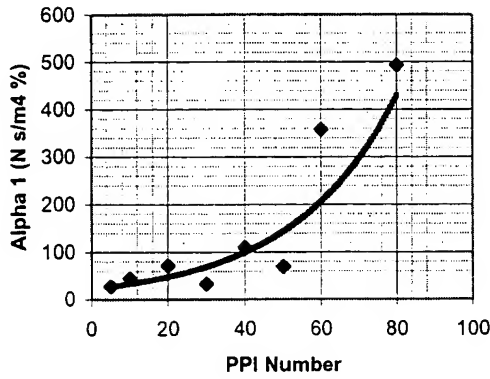
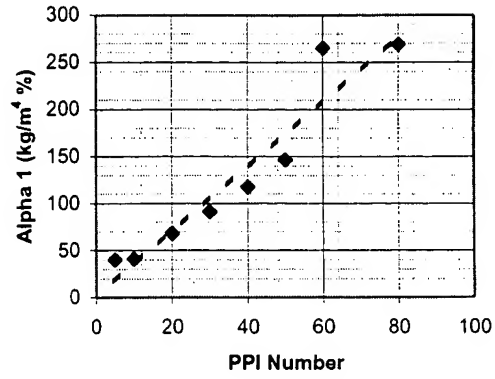


Figure 7: α_2 as a Function of PPI Number



The coefficient α_1 was found to have an exponential dependence on the ppi number while the coefficient α_2 was found to have a linear dependence on the ppi number. Finally, an equation was developed to quantify the coefficients of Eq. 4. They are as follows:

$$\frac{\mu}{K} = 19.5734 \rho_{rel} e^{0.0364(ppi)} \quad (14)$$

$$C\rho = 2.93598 \rho_{rel} (ppi) \quad (15)$$

Figure 8 shows the relationship between the actual pressure drop and the model generated from Eq. 4, Eq. 14, and Eq. 15 (Model I). The chart indicates a coefficient of determination of 91.2% implying that the model accounts for approximately 91% of the variation in the actual data. A slightly more complex adaptation of Eq. 14 and Eq. 15 was explored yielding a coefficient of determination of 96.2%. The adaptation is as follows: occurrences

$$\frac{\mu}{K} = 13.6173 \rho_{rel}^{2.06} e^{0.0364(ppi^{0.63})} \quad (16)$$

$$C\rho = 2.046 \rho_{rel}^{2.06} ppi^{0.63} \quad (17)$$

Figure 9 shows the relationship between actual pressure drop and the model generated from Eq. 4, Eq. 16, and Eq. 17 (Model II).

Figure 8: Model I (Eq 4, 14, & 15) vs Actual

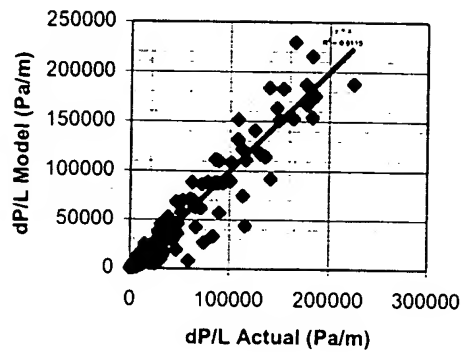
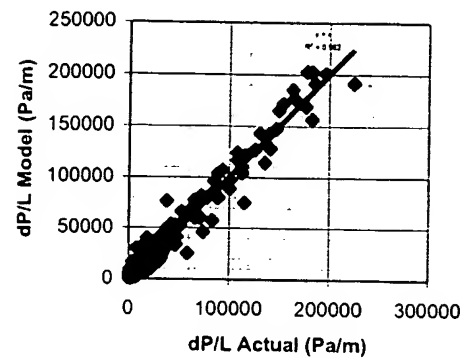


Figure 9: Model II (Eq 4, 16, & 17) vs Actual



The maximum deviation from Model I is 71,704 pascals per meter, while the maximum deviation from Model II of the data shown in Figure 8 is 40,258 pascals per meter. In an effort to understand if the variation can be attributed to any of the recorded test parameters, an analysis of variance (ANOVA) is conducted for air velocity, material diameter, material density, ppi, and material thickness. The following hypothesis was tested:

H_0 : There is no difference in the model deviation means

H_a : At least two of the model deviation means differ.

The complete results from the ANOVA along with the histograms of the variable categories are in Appendix III. The analysis shows that there is sufficient evidence (at 99% confidence) to reject H_0 for all the variables categories investigated in Model I. Rejection of the null hypothesis indicates that the model deviation average for the categories differ; therefore some of the model deviation can be attributed to each of the categories investigated. The ANOVA for Model II indicates that the null hypothesis cannot be rejected for density and thickness, suggesting there is not sufficient evidence that the model deviation can be attributed to these two parameters. The analysis is summarized in Table 1.

Table 1: ANOVA Results

Recorded Parameter	Model I		Model II	
	F Statistic	Conclusion	F Statistic	Conclusion
Density	4.785	Reject H_0 w/ 99% Conf.	0.338	Accept H_0
PPI	3.38	Reject H_0 w/ 95% Conf.	5.696	Reject H_0 w/ 99% Conf.
Air Velocity	20.075	Reject H_0 w/ 99% Conf.	6.70	Reject H_0 w/ 99% Conf.
Thickness	6.3526	Reject H_0 w/ 99% Conf.	2.081	Accept H_0
Diameter	12.382	Reject H_0 w/ 99% Conf.	5.113	Reject H_0 w/ 99% Conf.

Based on the ANOVA results, an adaptation of Model II is developed in an effort to capture as much of the variance in the data as possible. Model III accounts for the variation in hydraulic diameter, allows the velocity exponents to vary, and also allows for dissimilar exponents in PPI and relative density. The model coefficient of determination is approximately 99% and takes the form:

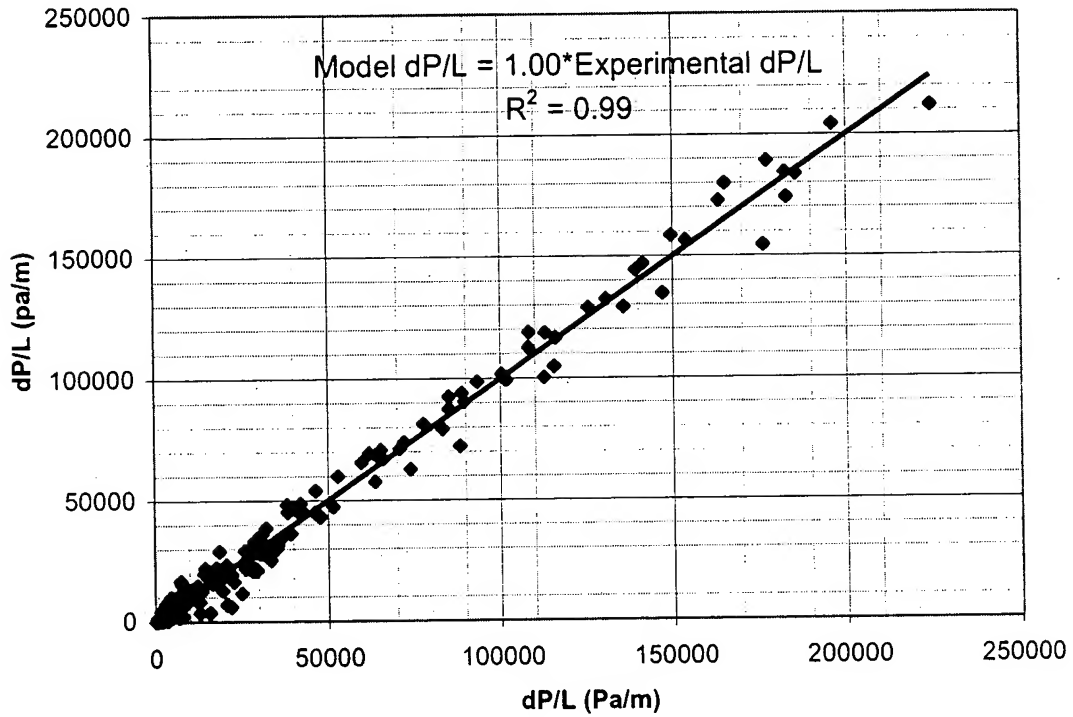
$$\frac{\Delta P}{L} = \frac{1}{D^{1.559}} \left[\frac{\mu}{K} U^2 + \rho C U^{0.128} \right] \quad (18)$$

$$\frac{\mu}{K} = 3.176 \times 10^{-2} \rho_{rel}^{2.09} e^{0.131(ppi)^{0.59}} \quad (19)$$

$$C\rho = 4.764 \times 10^{-3} \rho_{rel}^{2.03} ppi^{1.22} \quad (20)$$

Eq. 18 indicates that as the diameter is decreased, the pressure drop increases. The diameter interaction seems to make physical sense as well as helping to increase the coefficient of determination for the model. The graph of Model III with the experimental results is shown in Figure 10.

Figure 10: Model III Pressure Drop vs Experimental Pressure Drop

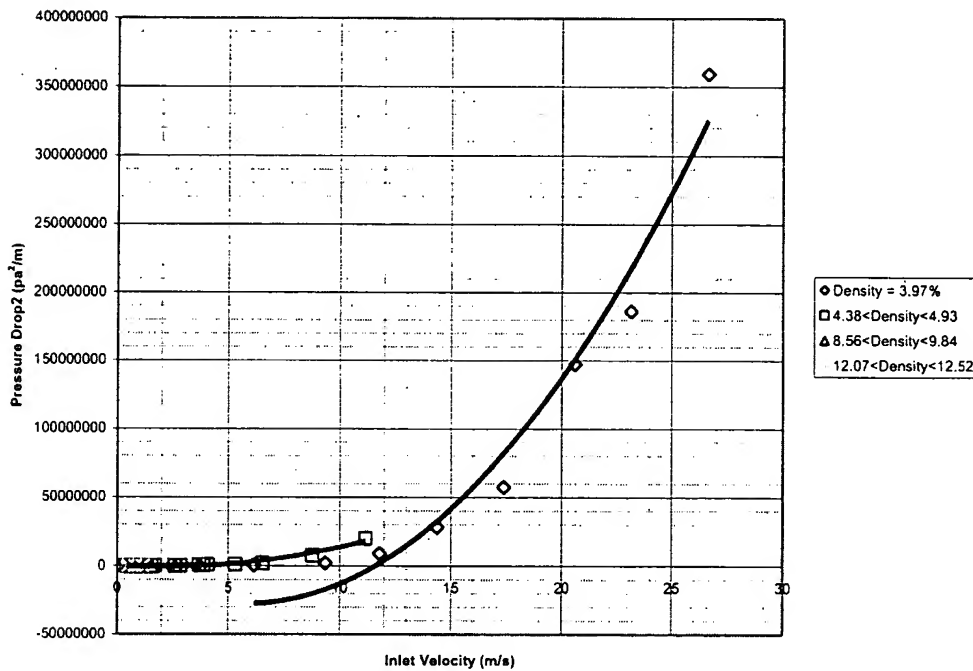


Scrutiny of Eq. 9

The next step in the analysis is to determine the feasibility of using Eq. 9 to determine the pressure drop dependence. Figure 11 shows the relationship between the pressure drop squared as a function

of velocity. The curve does not fit the physics of the problem and allows a negative pressure drop at low flows. The same trend is observed at foams with higher ppi number and relative density, these charts can be found in Appendix IV. For this reason, Eq. 9 is excluded from further scrutiny and SHOULD NOT be used to calculate the pressure drop in metal foams. The chart also illustrates that as the pressure drop increases, Eq. 9 does a good job at determining the velocity/pressure drop relationship. Eq. 9 was developed for use in sintered metal beds rather than metal foams. Since the pressure drop in sintered beds is much higher than in metal foams the equation probably works much better in that application.

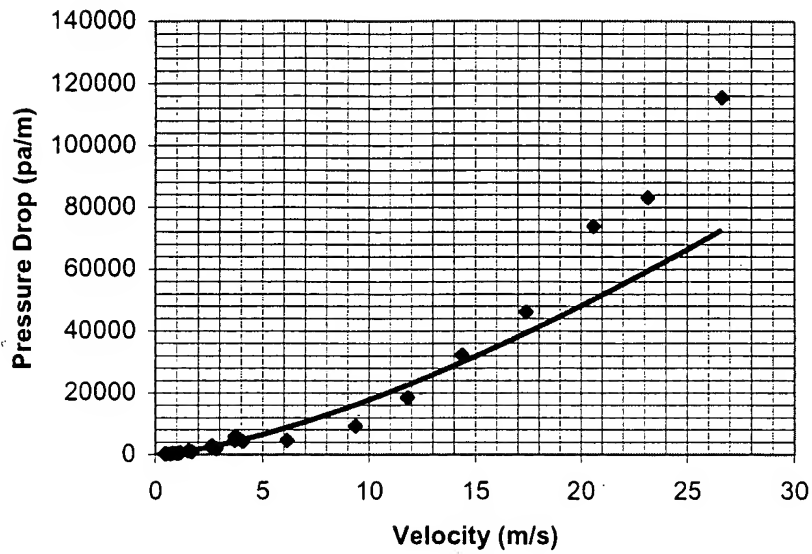
**Figure 11: Pressure Drop² as a Function of Inlet Velocity
5 ppi, Various Relative Densities**



Scrutiny of Eq. 11

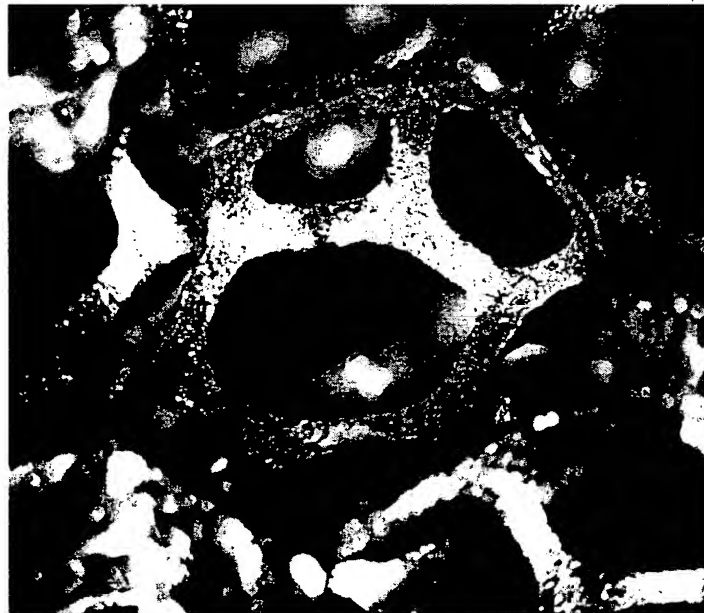
The last relationship studied is Eq. 11. After looking at Eq. 18, one can see that the most dominant term in the pressure drop equation is U^2 . Therefore, it is not a far stretch of the imagination to believe that a single velocity term could yield a good fit to the experimental data. Figure 12 shows the experimental data fit with a power law curve.

Figure 12: Pressue Drop as a Function of U^k



Another interesting relationship can be derived from the data in conjunction with another experimental measurement. Stainless steel metal foam was photographed in order to obtain the dependence of ppi and density on the strut diameter. A grid was over-laid on the sample, the pore size and strut diameter was measured with a ruler and scaled appropriately. Figure 13 shows a picture of the cell and the connecting struts.

Figure 13: Microscope Picture of Metal Foam

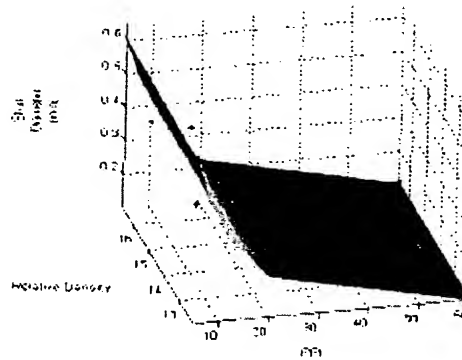


Based on the results, the strut diameter is proportional to relative density and inversely proportional to ppi. The relationship is found to follow,

$$d = 1.4 \frac{\rho_{rel}^{0.1}}{ppi^{0.7}}, \quad (21)$$

Figure 13 shows a good fit with the experimental data.

Figure13: Strut Diameter Model Compared to Actual Data

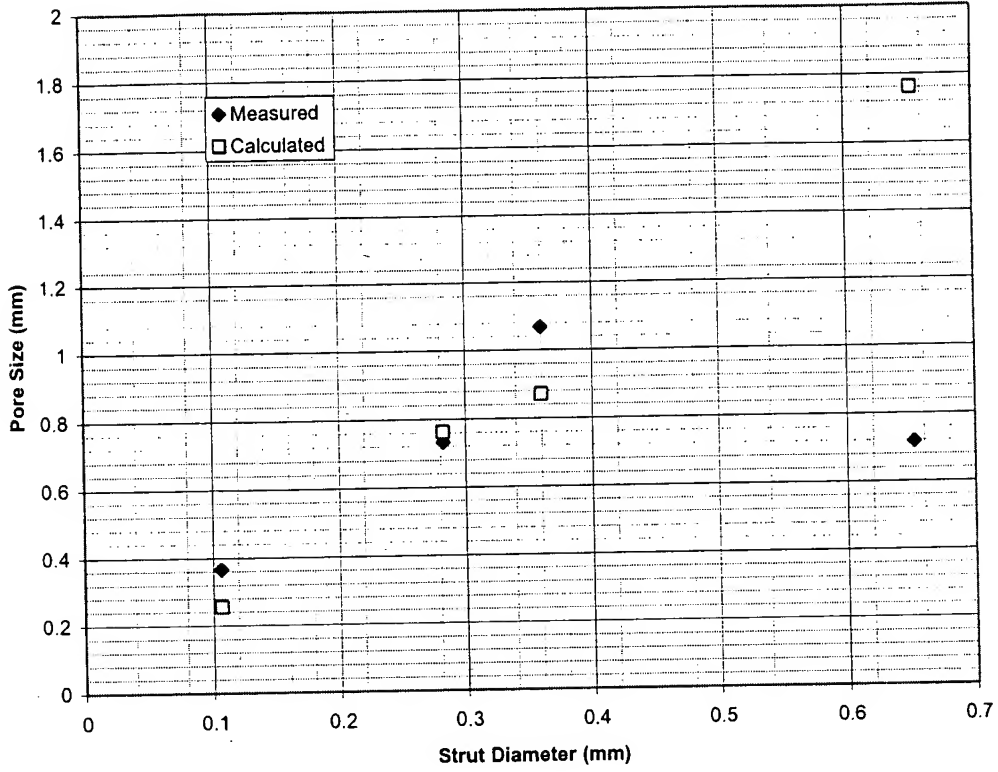


The pore diameter is related to the strut diameter as:

$$a = \frac{d}{\sqrt{\frac{\rho_{rel}}{100}}} \left[1 - e^{\frac{-\rho_{rel}}{0.0004}} \right]. \quad (22)$$

The comparison of the actual to calculated is shown in Figure 14.

Figure 14: Experimental and Calculated Pore Size as a Function of Strut Diameter



Finally, based on Eq. 10, Eq. 11, Eq. 21, and Eq. 22, we derive the dependence of pressure drop on ppi, relative density, and velocity. The equation takes the form:

$$\frac{\Delta P}{L} = \hat{\xi} \left[\frac{\rho_{rel}^{0.4-0.1m}}{1 - e^{\frac{-\rho_{rel}}{0.04}}} \right] \left[\frac{v_a^m \rho_a}{(1-\alpha)^{2-m}} \right] U_f^{2-m} (ppi^{0.7+0.7m}). \quad (23)$$

Using a curve fitting algorithm, we see that $m=0.19$ and $\hat{\xi}=182.595$.

Comparison of Stainless Steel Pressure Drop to FeCrAlY Pressure Drop

Since the sintering properties of stainless steel and FeCrAlY are similar, one would expect that the strut diameter, pore size, and consequently, the pressure drop, would be similar as well. The strut diameter and pore size was determined by Cambridge University for FeCrAlY using image analysis. The dependence of the strut diameter on ppi and relative density from their report, is found to be

$$d = 0.601359 \frac{\rho_{rel}^{0.19}}{ppi^{0.41}} \quad (24)$$

Eq. 24 is subtracted from Eq. 21 and then divided by Eq. 21 to give the relative difference in strut diameter and is shown in Figure 15. The plot indicates that the relative difference is small at low ppi, but increases as ppi increases.

Figure 15: Relative Difference in Strut Diameter Compared to ppi and Relative Density

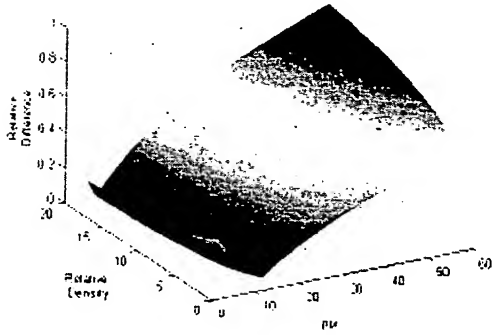
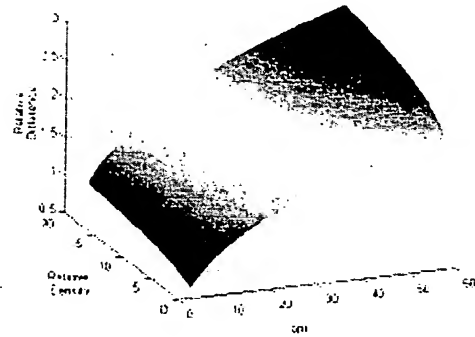


Figure 16: Relative Difference in Cell Diameter Compared to ppi and Relative Density



Also, the cell diameter is found to fit the equation,

$$a = \frac{\sqrt{3}\pi}{1.18} \frac{d}{\sqrt{\rho_{rel}}} \left[1 - e^{\frac{-\rho_{rel}}{0.0004}} \right] \quad (25)$$

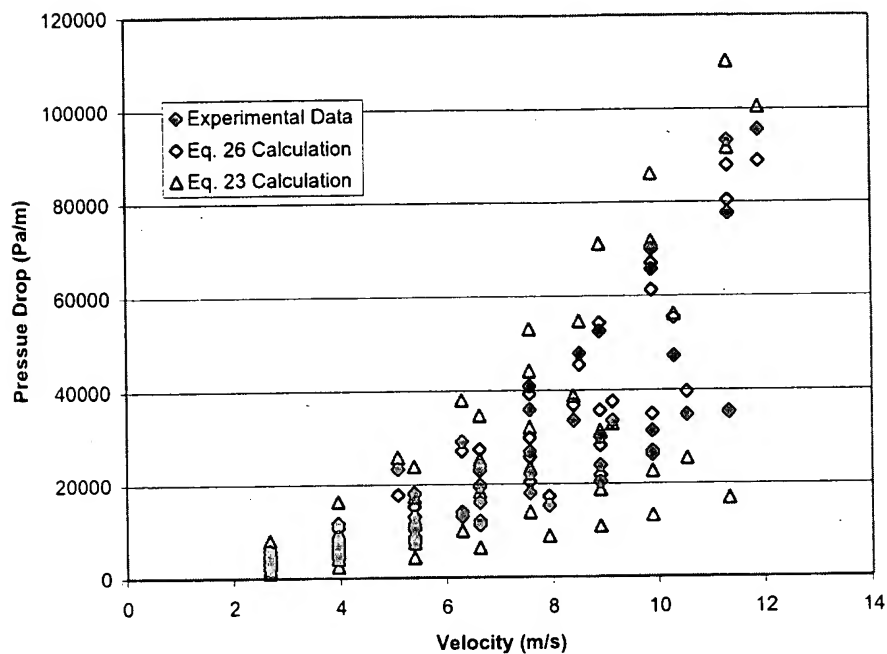
Eq. 25 is subtracted from Eq. 22 and then divided by Eq. 22 to give the relative difference in cell diameter and is shown in Figure 16. Again, the plot indicates that the relative difference is small at low ppi, but increases as ppi increases.

Due to the calculated differences in the strut diameter and cell size, Eq.10 is used in conjunction with Eq. 24 and Eq. 25. The resultant equation,

$$\frac{\Delta P}{L} = \bar{\xi} \left[\frac{\rho_{rel}^{0.31-0.19\bar{m}}}{1 - e^{\frac{-\rho_{rel}}{0.04}}} \right] \left[\frac{v_a^{\bar{m}} \rho_a}{(1-\alpha)^{2-\bar{m}}} \right] U_f^{2-\bar{m}} (ppi^{0.41+0.41\bar{m}}), \quad (26)$$

is used in a curve fitting algorithm indicating $\bar{\xi} = 4.219 \times 10^6$ and $\bar{m} = 0$. Although the values of the constants in Eq. 26 and Eq. 23 are much different, the results from the equations are not much different for one another. Figure 17 shows the results of using the stainless steel correlation (Eq. 23) to predict the pressure drop in FeCrAlY.

Figure 17: Using the Stainless Steel Calculation to Predict the Pressure Drop in FeCrAlY

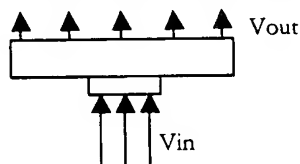


The chart shows that the stainless steel prediction possesses the same trend and magnitude as the FeCrAlY prediction. Since the pressure drop of the two materials is so much alike, one would expect that the material pore sizes and cell diameters are much alike as well. Therefore, the data suggests that the strut diameter and pore size measured manually differs from those obtained from image analysis. Further measurements should be taken to understand why there is a difference.

Experimental Results For Differing Inlet and Exit Diameter

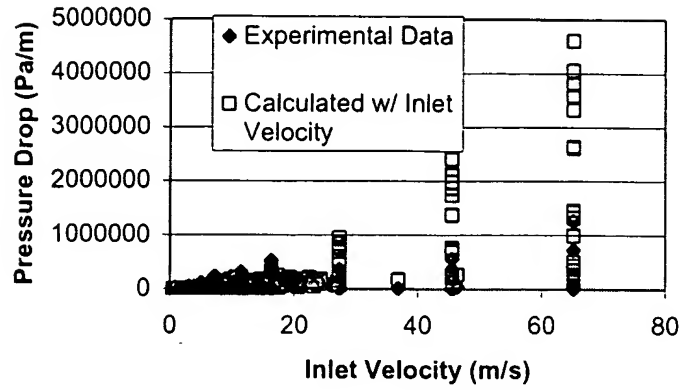
In all the preceding results, the inlet diameter and exit diameter of the part was kept constant thereby keeping the air velocity constant. The question arises, "If the velocity of the stream through a metal foam changes along its length, which velocity should be used in the above equations, the inlet, the exit, or an average?" In order to answer this question, an apparatus was constructed with an inlet orifice placed in front of the metal foam part, shown schematically in Figure 18.

Figure 18: Schematic of Testing Apparatus



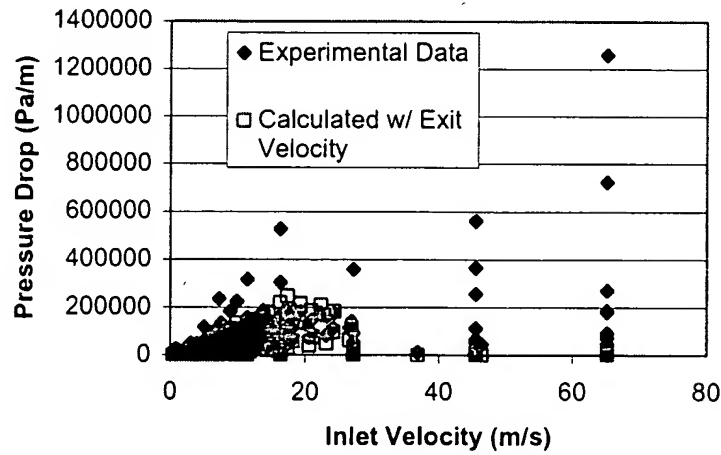
The inlet orifice diameter, inlet velocity, metal foam diameter, metal foam thickness, metal foam relative density and ppi were all varied. The experimental pressure drop versus the calculated pressure drop was plotted using the inlet velocity and exit velocity. These plots are shown in Figures 18 and 19.

Figure 18: Experimental Pressure Drop Compared to Calculated w/ Inlet Velocity



One can see from Figure 18 that the inlet velocity gives fair accuracy at low velocities, but at high inlet velocities the pressure drop is overestimated.

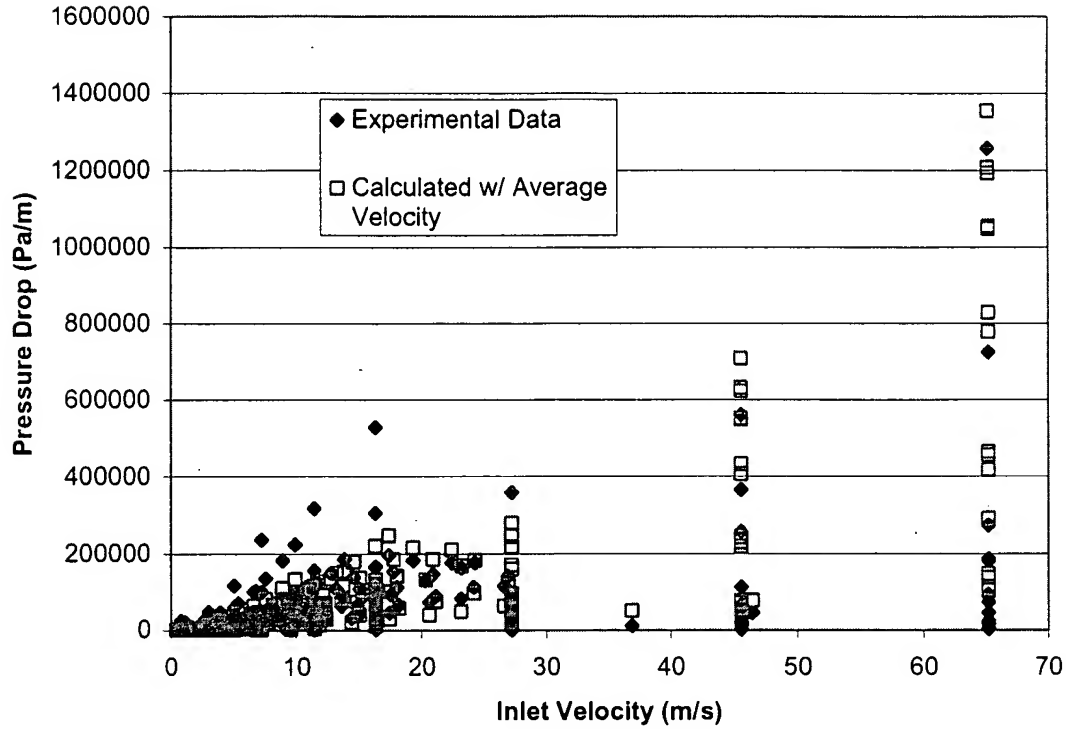
Figure 19: Experimental Pressure Drop Compared to Calculated w/ Exit Velocity



Conversely, one can see that the pressure drop is underestimated when using the exit velocity in the pressure drop equation. Due to the inaccuracy in the pressure drop prediction, it becomes necessary to develop a velocity-averaging scheme to generate a velocity to be used in the pressure drop equations.

As an initial pass, a simple average is taken $(U_{fin} + U_{iout})/2$. The results are shown in Figure 20.

Figure 20: Experimental Pressure Drop Compared to Calculated w/ Average Velocity



In order to determine if the error can be improved on, the weighted average function,

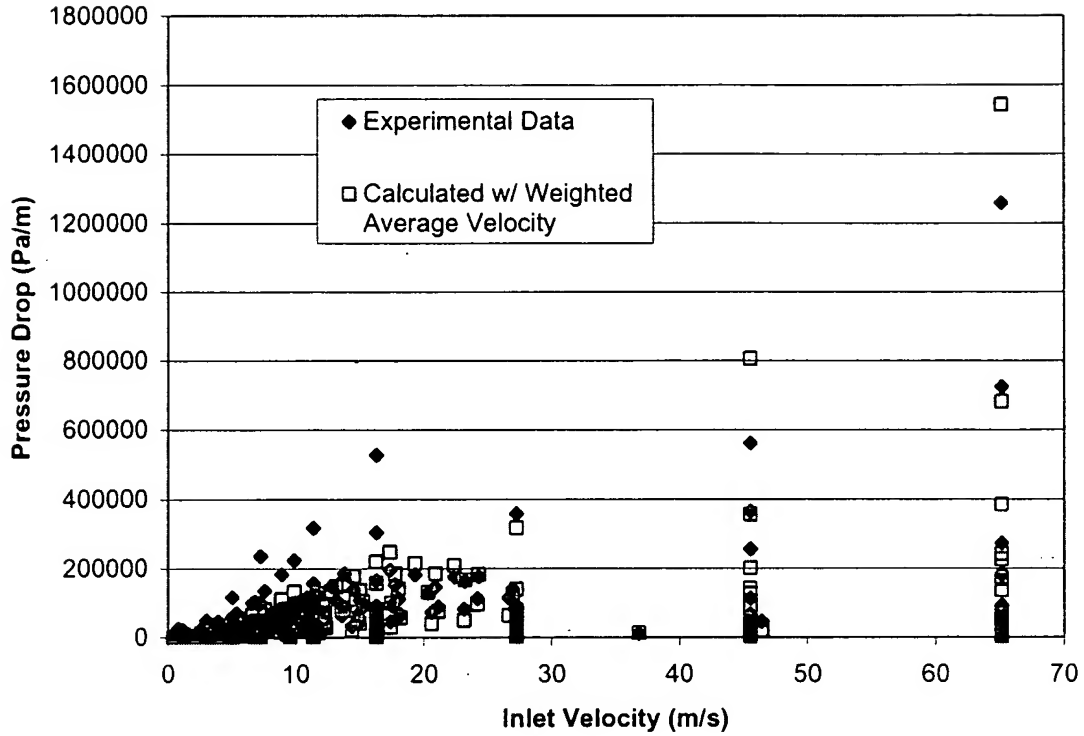
$$\bar{U}_f = kU_{f_{in}} + (1-k)U_{f_{out}}, \quad (27)$$

along with the weighting function,

$$k = \left[\left(1 - \frac{ppi}{200} \right)^{-1.8} \left(1 - \frac{\rho_{rel}}{100} \right)^{-9.8} \left(1 - \frac{L}{1} \right)^{13.964} \right]^{0.74} \left(1 - \frac{D_{in}}{D_{out}} \right), \quad (28)$$

is used to calculate the pressure drop. The values for the exponents were arrived at through a curve fitting algorithm which maximized the R^2 value when the calculated pressure drop was plotted with the experimental pressure drop. These results from the more complex averaging function are shown in Figure 21. The chart indicates that the simple averaging function is not a bad approximation when determining the pressure drop.

**Figur 21: Experim ntal Pressure Drop Compared to
Calculated w/ Weighted Average V locity**



VELOCITY PROFILES IN IRON BASED METAL FOAMS

In applications where metal foams are used for flow diffusion, the velocity profiles at the exit of the material are of interest. Measurements were taken in an attempt to determine the exit velocity profile and its dependence on the incoming velocity, the part diameter, part length, the ppi, and the relative density. Figure 22 and 23 show a typical velocity profile for a 5ppi, 12% relative density stainless steel part with a 1/2 inch inlet orifice and a 3.75 in part exit. If the velocity is plotted as a function of distance, a Gaussian profile emerges (Figure 24). The maximum velocity and the velocity scatter can then quantify the velocity contour allowing us to see trends when parameters are varied. In general, the profile distribution is assumed to follow

$$U_{f,r} = U_{f,max} e^{\frac{-r^2}{2\sigma}} \quad (29)$$

The values of $U_{f,max}$ and 2σ are shown in Figure 24 for the particular case.

Figure 22: Exit Velocity Contour for a 5ppi, 12% Relative Density Stainless Steel w/ 0.5" Inlet Diameter and 3.75" Exit Diameter

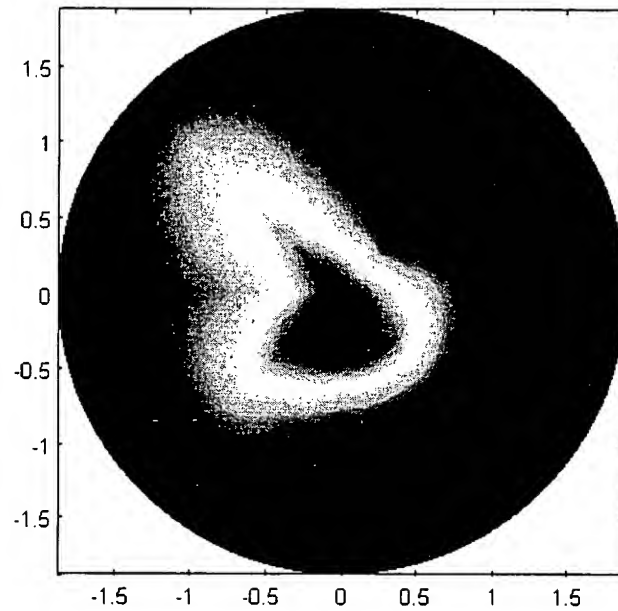


Figure 23: Exit Velocity Surface for a 5ppi, 12% Relative Density Stainless Steel w/ 0.5" Inlet Diameter and 3.75" Exit Diameter

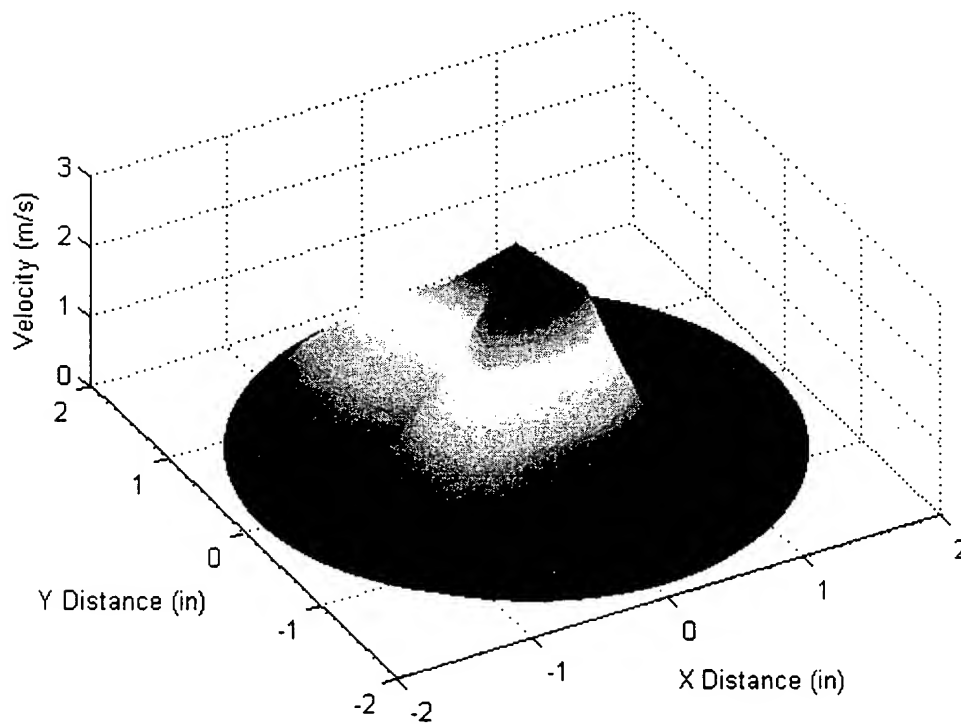
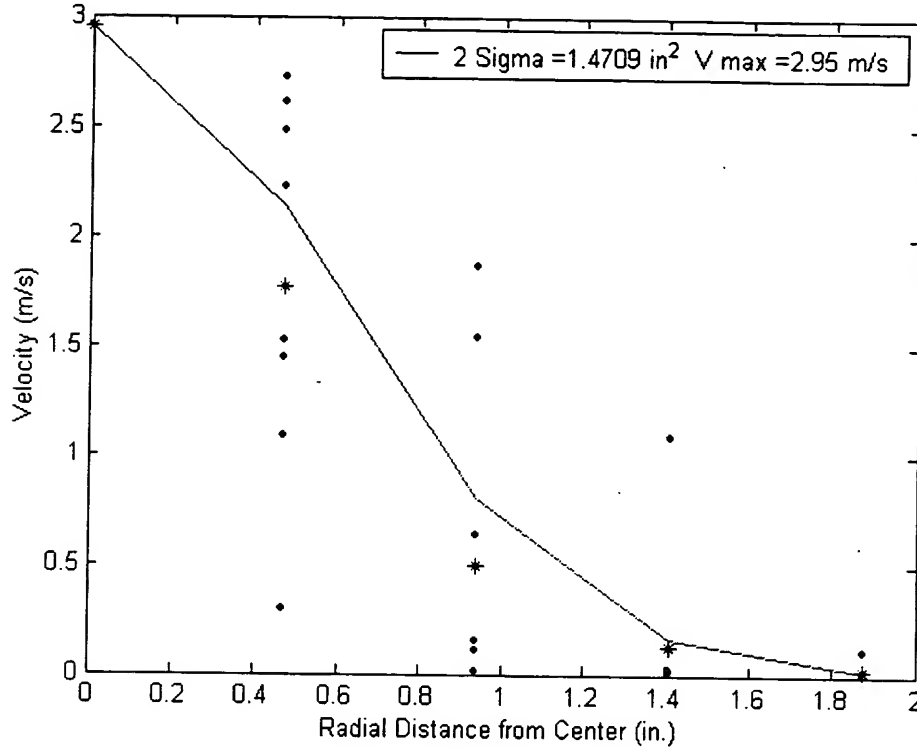


Figure 24: Exit Velocity Profile for a 5ppi, 12% Relative Density Stainless Steel w/ 0.5" Inlet Diameter and 3.75" Exit Diameter
Average Velocity (Blue Stars) Compared to Gaussian Distribution (Green Line)



We can determine $U_{f_{max}}$ by conservation of momentum and by integrating the proposed velocity profile. $U_{f_{max}}$ is shown below in terms of the other variables.

$$U_{f_{max}} = 2 \left(\frac{D_1}{D_2} \right)^2 U_{f_{in}} \frac{1}{\sqrt{2\pi\sigma}}. \quad (30)$$

It also reasonable to believe that 2σ is a function of the foam thickness, ppi, relative density, inlet velocity and diameter. A multiple variable non-linear curve fit was conducted to determine the dependence of 2σ on the independent variables. The following relationship emerges,

$$2\sigma = 3.513 \left(\frac{D_2}{D_1} \right)^{1.08} \left(\frac{1}{U_{f_{in}}^{0.06} ppi^{0.6} \rho_{rel}^{0.66} L^{3.09}} \right), \quad (31)$$

however, the coefficient of determination is small ($R^2=30\%$) and can yield significant scatter from the experimental data. It is recommended that computational fluid dynamics be used if accuracy is required. Eq. 31 is intended to give a the flow scatter trends rather than the actual values.

SUMMARY

The relationships for pressure drop as a function of velocity are presented. The set of equations with the largest coefficient of determination at 99% is:

$$\frac{\Delta P}{L} = \frac{1}{D^{1.559}} \left[\frac{\mu}{K} U^2 + \rho C U^{0.128} \right] \quad (18)$$

$$\frac{\mu}{K} = 3.176 \times 10^{-2} \rho_{rel}^{2.09} e^{0.131(ppi)^{0.59}} \quad (19)$$

$$C\rho = 4.764 \times 10^{-3} \rho_{rel}^{2.03} ppi^{1.22} \quad (20)$$

Eq. (18), (19), and (20) yield good results over a range of PPI, relative density, thickness, and part diameter. In general Eq. (19) and (20) vary depending on the material. Therefore the values of $\frac{\mu}{K}$ and $C\rho$ must be regressed for the different materials used.

With some loss in accuracy, but gaining a generalized formula for all materials, the following equation is used:

$$\frac{\Delta P}{L} = \xi \frac{1}{a} \left[\frac{v_a^m \rho_a}{(1-\alpha)^{2-m}} \right] U_f^{2-m} d^{-m} \quad (10)$$

where the cell diameter and the strut size of the material are the variables used to dictate the pressure drop.

The strut size of stainless steel is found to follow the relationship,

$$d = 1.4 \frac{\rho_{rel}^{0.1}}{ppi^{0.7}}, \quad (21)$$

and the cell diameter can be described by

$$a = \frac{d}{\sqrt{\frac{\rho_{rel}}{100}}} \left[1 - e^{\frac{-\rho_{rel}}{0.04}} \right]. \quad (22)$$

There are conflicting results for the strut size and cell diameter of FeCrAlY when calculated manually and using visual analysis software, but using Eq. (21) and (22) in Eq. (10) yields approximately the same results as the experimental data for the pressure drop. Therefore, it is assumed that the strut diameter and cell diameter are close to those calculated for stainless steel.

In the case where the inlet and exit velocities differ, a velocity averaging scheme should be used. The best fit to the experimental data was found with the weighted average,

$$\bar{U}_f = kU_{f_{in}} + (1-k)U_{f_{out}}, \quad (27)$$

and the weighting function,

$$k = \left[\left(1 - \frac{ppi}{200} \right)^{-1.8} \left(1 - \frac{\rho_{rel}}{100} \right)^{-9.8} \left(1 - \frac{L}{1} \right)^{13.964} \right]^{0.74} \left(1 - \frac{D_{in}}{D_{out}} \right) \quad (28)$$

The velocity profile at the exit of the metal foam is found to follow the Gaussian distribution,

$$U_{f,r} = U_{f_{max}} e^{\frac{-r^2}{2\sigma}} \quad (29)$$

The constant $U_{f_{max}}$ is found through conservation of mass and the integration of Eq. (29) as

$$U_{f_{max}} = 2 \left(\frac{D_1}{D_2} \right)^2 U_{f_{in}} \frac{1}{\sqrt{2\pi\sigma}} \quad (30)$$

2σ is a function of the inlet velocity, the inlet diameter, the exit diameter, the PPI number, the relative density, and the thickness. A multiple variable non-linear curve fit yields the following relationship,

$$2\sigma = 3.513 \left(\frac{D_2}{D_1} \right)^{1.08} \left(\frac{1}{U_{f_{in}}^{0.06} ppi^{0.6} \rho_{rel}^{0.66} L^{3.09}} \right) \quad (31)$$

The R^2 value for this curve fit was low, but gives the trends for the maximum velocity and flow dispersion within metal foams.

Further testing on other materials such as titanium and nickel is being carried out to fully develop pressure drop and flow profile equations for a wide range of alloys.

Appendix I: Pressure Drop as a Function of Velocity

Appendix II: Coefficients for Velocity Terms in Eq. 4

PPI Number	Relative Density (%)	μ/K (N s/m ⁴)	ρC (kg/m ⁴)
5	3.97	160.7396	1.00E-05
5	4.66	221.7	218.35
5	9.2	349.71	260
10	4.18	194.74	1.00E-05
10	4.31	242.63	420
10	16.5	654.86	731.66
20	4.7	286.23	392.62
20	7.7	739.84	619.62
20	9.5	442.16	75.754
20	10	607.84	1451.5
20	12.5	944.39	694.72
30	4.1	342.94	96.617
30	4.4	431.82	180.24
40	4.8	482.94	0
40	5.5	508.61	715.18
50	4.5	557.02	870.11
60	4.4	585.67	841.57
60	5.4	720.62	2257.4
60	7.9	565.38	5287.9
60	8.9	1969.2	2437.8
60	11.1	2194.1	410.47
60	13.3	11220	4699.2
60	16.7	110.97	7722
60	7.1	1910.4	3505.1

Appendix III: Avova Analysis

Appendix IV: Pressure Drop Squared as a Function of Velocity

THIS PAGE BLANK (USPTO)